

# 1 Microbial U isotope fractionation depends on U(VI) 2 reduction rate

3 *Anirban Basu*<sup>1\*</sup>, *Christoph Wanner*<sup>2</sup>, *Thomas M. Johnson*<sup>3</sup>, *Craig C. Lundstrom*<sup>3</sup>, *Robert A.*  
4 *Sanford*<sup>3</sup>, *Eric L. Sonnenthal*<sup>4</sup>, *Maxim I. Boyanov*<sup>5,6</sup>, *Kenneth M. Kemner*<sup>5</sup>

5

6 1. Department of Earth Sciences, Royal Holloway, University of London, Egham, UK, TW20  
7 0EX

8 2. Institute of Geological Sciences, University of Bern, Baltzerstrasse 3, CH-3012, Switzerland

9 3. Department of Geology, University of Illinois at Urbana-Champaign, Urbana, IL, USA 61801

10 4. Lawrence Berkeley National Laboratory, 1 Cyclotron Road, Berkeley, CA, USA, 94720

11 5. Biosciences Division, Argonne National Laboratory, Argonne, IL, USA, 60439

12 6. Bulgarian Academy of Sciences, Institute of Chemical Engineering, Sofia 1113, Bulgaria

13

14

15

16 **KEYWORDS:** Uranium isotopes, bacteria, U(VI) reduction rate, numerical simulations

## 17 ABSTRACT

18 U isotope fractionation may serve as an accurate proxy for U(VI) reduction in both modern and  
19 ancient environments, if the systematic controls on magnitude of fractionation ( $\epsilon$ ) are known. We  
20 model the effect of U(VI) reduction kinetics on U isotopic fractionation during U(VI) reduction  
21 by a novel *Shewanella* isolate, *Shewanella* sp. (NR) in batch incubations. The measured  $\epsilon$  values  
22 range from  $0.96\text{‰} \pm 0.16$  to  $0.36\text{‰} \pm 0.07\text{‰}$  and are strongly dependent on the U(VI)  
23 reduction rate. The  $\epsilon$  decreases with increasing reduction rate constants normalized by cell  
24 density and initial U(VI). Reactive transport simulations suggest that the rate dependence of  $\epsilon$  is  
25 due to a two-step process, where diffusive transport of U(VI) from the bulk solution across a  
26 boundary layer is followed by enzymatic reduction. Our results imply that the spatial decoupling  
27 of bulk U(VI) solution and enzymatic reduction should be taken into account for interpreting U  
28 isotope data from the environment.

## 29 INTRODUCTION

30 The uranium isotope ratio  $^{238}\text{U}/^{235}\text{U}$  is an effective proxy for understanding microbially-  
31 mediated uranium (U) reduction, which is an integral part of the global U cycling throughout  
32 geologic time. Bacterial reduction of soluble U(VI) to insoluble U(IV) leads to preferential  
33 partitioning of  $^{238}\text{U}$  in the U(IV) solids with lowest possible electron density configuration at the  
34 nucleus<sup>1-3</sup>. This equilibrium isotopic exchange resulting from the differences in nuclear size and  
35 shape is described in the literature as a nuclear volume effect (NVE)<sup>4,5</sup>. However, it is not clear  
36 how and at which rate the exchange occurs during kinetically controlled and irreversible  
37 microbial reduction. With continued bacterial reduction, the residual aqueous U(VI) becomes  
38 progressively enriched in  $^{235}\text{U}$ . Direct measurement of  $^{238}\text{U}/^{235}\text{U}$  permits the quantification of U  
39 cycling in both modern and ancient environments such as contaminated aquifers<sup>6,7</sup> and the rock

40 record<sup>8</sup>, but this is predicated on a robust understanding of the factors that control the magnitude  
41 of U isotopic fractionation during microbial U(VI) reduction.

42 The magnitude of U isotope fractionation caused by bacterial U(VI) reduction is variable.  
43 Generally, it is expressed as the enrichment factor  $\epsilon$  ( $\epsilon$  (‰) =  $1000 * (\alpha - 1)$ ;  $\alpha = (R_{\text{instantaneous U(VI)}}$   
44  $\text{product} / R_{\text{U(VI)}})$  where R is  $^{238}\text{U} / ^{235}\text{U}$ ). A field-scale biostimulation of a U(VI) contaminated aquifer  
45 at Rifle, CO, USA, has yielded an apparent fractionation (as  $\epsilon$ ) of 0.46‰<sup>9</sup>. Laboratory batch  
46 incubations with a diverse group of bacteria have revealed a range of  $\epsilon$  from 0.7‰ to 1.0‰<sup>1</sup>.  
47 Subsequent experimental work has reported a similar range for batch incubations with single  
48 strains<sup>2,3</sup>. The large variability of  $\epsilon$  translates to large uncertainties in determining the fraction of  
49 reduction of toxic U(VI) in contaminated aquifers<sup>9-11</sup> or the extent of anoxia in ancient oceans<sup>12</sup>,  
50 which makes the interpretation of the environmental U isotope data equivocal. To date, the  
51 origins and nature of variability of  $\epsilon$  for microbial U(VI) reduction has not been fully explored.  
52 For similar redox-active elements like S and N, however, the variation of  $\epsilon$  is systematically  
53 controlled by the rate of microbial sulfate and nitrate reduction (e.g. ref. <sup>13,14</sup>).

54 The key role of bacterial physiology in controlling the S isotopic fractionation by sulfate  
55 reducers is well understood<sup>13,15,16</sup>. One crucial factor that controls the S isotope fractionation is  
56 the balance between the rate of sulfate delivery into the cell and the rate of sulfate reduction in  
57 the cell<sup>13,17</sup>. The fractionation is maximized when the transport of sulfate into the cell is  
58 unlimited and the electron donor supply is limited leading to slow reduction<sup>13</sup>. In contrast, when  
59 the supply of sulfate is low relative to the supply of the electrons such that the supplied sulfate is  
60 rapidly, and nearly quantitatively, reduced, the S isotopic fractionation diminishes to zero. The  
61 balance between the reduction rate and supply of sulfate depends on the components of  
62 enzymatic reaction machinery and the electron transport chain. Similarly, we expect that

63 microbial U isotopic fractionation may be influenced by the rate of U(VI) reduction relative to  
64 the rate of U(VI) supply, despite differences in mechanisms of U(VI) reduction and cellular  
65 transport of U(VI).

66 Bacterial strains from the *Shewanella* genera are particularly well-studied for their U(VI)  
67 reduction ability, which has generally been attributed to membrane-associated enzymes –c-type  
68 cytochromes associated with the outer membrane or the periplasmic space<sup>18-22</sup>. Consequently, the  
69 U(IV) reaction products are observed to form outside the cell, on the cell membrane and in the  
70 periplasmic space in several *Shewanella* species<sup>21,23</sup>. Therefore, the localization of U(VI)  
71 reduction in the vicinity of the outer-membrane or periplasmic enzymes may influence the  
72 balance between the U(VI) delivery and reduction rate.

73 Here we demonstrate the effect of variable U(VI) reduction rates on the magnitude of isotopic  
74 fractionation in batch incubation experiments with *Shewanella* sp. (NR). We varied the initial  
75 U(VI) concentration while keeping other parameters (e.g. electron donor concentration, cell  
76 density) the same and we determined the magnitude of isotopic fractionation. We propose a two-  
77 step mechanistic model of U isotopic fractionation with diffusive delivery of aqueous U(VI)  
78 followed by enzymatic U(VI) reduction. In this model, we consider a diffusive boundary layer  
79 surrounding the cell separating a region of enzymatic reduction from the bulk U(VI) solution.  
80 We test this conceptual model by reactive transport simulations of U(VI) reduction by  
81 *Shewanella* sp. (NR) to demonstrate the role of reaction kinetics in controlling the overall  
82 isotopic fractionation.

## 83 METHODS

### 84 *Media for Bacterial Cultures and U(VI) Incubations*

85 *Shewanella* sp. (NR) cultures were grown anaerobically in 80-100 mL batch cultures at 30°C  
86 using a mineral-salt media described in ref. <sup>1</sup>. Briefly, the medium contained 200 μM phosphate  
87 and 10 mM of HCO<sub>3</sub><sup>-</sup> buffer with a final pH of 7.2. The cultures were grown on 2.5 mM lactate  
88 as electron donor and 1 mM NO<sub>3</sub><sup>-</sup> as electron acceptor. The medium for U(VI) incubation  
89 experiments was identical to the growth medium except that the phosphate concentration was  
90 lowered to 20 μM to avoid abiotic U(VI)-phosphate precipitation. All reductants, vitamin  
91 solution and resazurin were omitted from both growth and test medium.

### 92 ***U(VI) Incubation Experiments***

93 A uranyl carbonate solution in 100 mM NaHCO<sub>3</sub>, prepared from Uranium (normal) metal  
94 CRM 112-A, was routinely used as U(VI) stock solution for desired initial U(VI) concentration  
95 in our experiments<sup>1</sup>. Each experiment was conducted in duplicate. A ~10 mL inoculum (10%  
96 v/v) of pre-grown *Shewanella* sp. (NR) was used for each experiment. The density of the  
97 microbial population in each reactor and the inoculum was quantified using a LSR II (BD  
98 Biosciences) flow cytometry analyzer. Abiotic control experiments with the test medium, the  
99 U(VI) bicarbonate solution and no bacteria were conducted for selected initial U(VI)  
100 concentrations. All reactors were supplemented with 500 μM of lactate as the electron donor.  
101 During the course of the experiments, all reactors were incubated at 30°C in the dark, shaken  
102 constantly at 125 rpm. Each reactor was sampled for U(VI) concentrations and U isotopes at  
103 regular intervals. The samples were filtered using 0.2 μm filters and stored at 4°C prior to  
104 analyses.

### 105 ***U Concentration and Isotope Measurements***

106 For isotopic analysis, we used a <sup>233</sup>U + <sup>236</sup>U double isotope spike technique to correct for any  
107 isotopic fractionation arising from sample purification or mass bias of the instrument during

108 mass-spectrometry. An aliquot of double isotope spike solution, composed of  $^{236}\text{U}$  and  $^{233}\text{U}$ , was  
109 added to each sample prior to sample purification by UTEVA resin<sup>1,6,7,9,24,25</sup>. Reported U(VI)  
110 concentrations were determined from isotope dilution calculations using measurements of spike  
111 isotopes and natural U isotopes in the samples. The  $\delta^{238}\text{U}$  values were measured using a Nu  
112 Plasma HR MC-ICP-MS. The precision of the isotopic measurements was 0.07‰, determined  
113 using a modified root mean square calculation<sup>26</sup> for 9 pairs of full procedural duplicate sample  
114 preparations. The relationship between isotopic composition and concentration from each set of  
115 U(VI) incubations was determined using a Rayleigh distillation equation

$$116 \quad \delta_t = (\delta_0 + 1000\text{‰}) \left[ \frac{c_t}{c_0} \right]^{\alpha - 1} - 1000\text{‰} \quad (1)$$

117 where  $c_0$  and  $\delta_0$  are the initial concentration and isotopic composition of U(VI),  $c_t$  and  $\delta_t$   
118 the concentration and isotopic composition at time  $t$ , and  $\alpha$  is the isotopic fractionation factor.  
119 The  $\alpha$  values were calculated from the slope of the best fit line from linearized plots of  $\ln(\delta^{238}\text{U} + 1000\text{‰})$   
120 vs.  $\ln(c_t)$ <sup>27</sup>. The uncertainties of  $\varepsilon$  (2\*standard error) were derived from the  
121 uncertainties of the slopes from data scatter about the best-fit lines using linear estimation  
122 method.

123 For experiments with early rapid U(VI) reduction, the sample taken a few minutes into each  
124 experiment is used as the effective starting point for  $\delta^{238}\text{U}$  and U(VI) concentration (see SI for  
125 more details). We also exclude some data from time points close to the completion of the  
126 reduction (e.g. >88% reduction for the experiment with  $\text{U(VI)}_{t=0} = 18.2 \mu\text{M}$ ) from our isotopic  
127 analysis. These data points are aberrantly shifted towards isotopically heavier values, which may  
128 be attributed to the contamination of the dissolved U(VI) solution by very fine U(IV) particles  
129 that later oxidize to U(VI).

### 130 ***Characterization of U(IV) precipitates***

131 Solid-phase associated U in the reactors was separated using a 0.2  $\mu\text{m}$  filter and analyzed using  
132 Uranium L<sub>III</sub>-edge X-ray absorption near-edge structure (XANES) at the MRCAT/EnviroCAT  
133 beamline, Advanced Photon Source, Argonne National Laboratory. The details of the analysis  
134 can be found in ref. <sup>28</sup> .

### 135 *Reactive transport modeling*

136 A series of reactive transport model simulations using TOUGHREACT V3<sup>29</sup> in combination  
137 with the EQ3/6 thermodynamic database<sup>30</sup> as well as uraninite solubility data taken from ref. <sup>31</sup> is  
138 performed to simulate U(VI) reduction and associated U isotopic fractionation. TOUGHREACT  
139 has been widely applied to evaluate isotopic fractionation coupled to water-rock interaction and  
140 biogeochemical processes in a variety of subsurface environments and laboratory  
141 experiments<sup>32,33</sup>. Furthermore, the TOUGHREACT approach for simulating isotopic  
142 fractionation coupled to redox reactions has been recently benchmarked<sup>34</sup>.

### 143 *Conceptual Model*

144 Our simplified conceptual model considers that cells are surrounded by boundary layers with  
145 U(VI) concentrations lower than those in the bulk solution (Fig. 1). Consequently, for our  
146 simulations we assume that U(VI) reduction occurs as a two-step process with (i) diffusive U(VI)  
147 transport through boundary layers and (ii) enzymatic U(VI) reduction at the cell surface or within  
148 the periplasmic space. A similar conceptual approach was successfully used by ref.<sup>32</sup> to  
149 demonstrate that Cr isotopic fractionation inherited from Cr(VI) reduction is muted if the  
150 reduction rate is high and/or diffusive transport is slow.

### 151 *Model Setup*

152 U(VI) reduction and associated U isotopic fractionation is simulated for a static batch reactor  
153 with no flow. A multi-region approach<sup>35</sup> is used to numerically formulate the conceptual model

154 (Fig. 1). To do so, the batch reactor is discretized into three different regions: (i) a bulk region  
155 corresponding to the U(VI) solution that is continuously sampled during the experiment, (ii) an  
156 enzyme region with enzymatic U(VI) reduction and (iii) a boundary region separating the  
157 previous two.

158 The physical parameters defined for the three regions are listed in Table S2 (Supporting  
159 Information). The simulations are performed for a model volume of 100 mL similar to that of the  
160 experiments. The volumes of the individual regions and mutual interfaces are defined assuming a  
161 cell density of  $10^7$  cells/mL, which is the average cell density of our experiments; a cuboid shape  
162 of *Shewanella* with a diameter of  $0.6 \mu\text{m}$  and length of  $3.4 \mu\text{m}$ <sup>36</sup>; and a boundary layer thickness  
163 of 20 nm. Although 20 nm approximately corresponds to the thickness of the entire Gram  
164 negative membrane of *Shewanella*<sup>37</sup>, we aim to simulate a general case where the location of  
165 U(VI) reduction is physically separated from the bulk U(VI) solution.

166 The cell density is kept constant during our simulations, meaning that we do not simulate  
167 microbial growth occurring in our experiments. The diffusive flux of U(VI) ( $J_D$ ) through the  
168 individual regions of our model (Fig. 1) is calculated according to

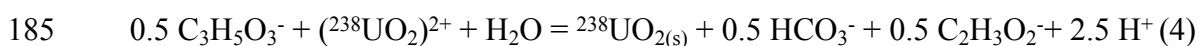
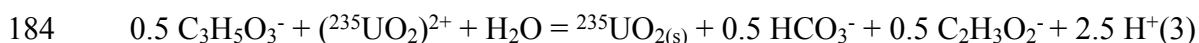
$$169 \quad J_D = D_{aq} \cdot \tau \cdot \phi \cdot \frac{A}{d_1 + d_2} \cdot \frac{dC}{dx} \quad (2)$$

170 where  $D_{aq}$  refers to the diffusion coefficient of aqueous species,  $A$  ( $\text{m}^2$ ) is the interfacial area  
171 between two adjacent regions,  $\frac{dC}{dx}$  refers to the U(VI) concentration gradient across a region  
172 ( $\text{mol}/\text{kg}_{\text{H}_2\text{O}}/\text{m}$ ),  $d_1$  and  $d_2$  refer to the distances from the centers of two adjacent regions to their  
173 mutual interface (Fig. 1),  $\tau$  is the tortuosity, and  $\phi$  is the porosity, which was set to 0.99. For the  
174 simulations it was assumed that the bulk region is fully mixed because the experiments were  
175 continuously stirred. Accordingly, the tortuosity of the bulk region was set to a very high value

176 of  $10^8$ . A value of  $10^8$  was also defined for the 1 nm thick enzyme region because we assume that  
 177 U(VI) is not further diffusively transported once it reaches a particular enzyme.

### 178 *Reaction network*

179 U(VI) reduction to U(IV) was assumed to occur exclusively within the enzyme region of our  
 180 model (Fig. 1). It was simulated as a kinetic reaction with lactate ( $C_3H_5O_3^-$ ) under the production  
 181 of  $HCO_3^-$  and acetate ( $C_2H_3O_2^-$ ) assuming that U(IV) immediately precipitates as uraninite  
 182 ( $UO_{2(s)}$ ). To simulate the fate of  $^{238}U$  and  $^{235}U$ , U(VI) reduction was defined for the two  
 183 dominating U(VI) and U(IV) isotopologues:



186  $^{235}UO_{2(s)}$  and  $^{238}UO_{2(s)}$  are defined as endmembers of an ideal uraninite solid solution with an  
 187 overall precipitation rate  $^{ss}r$  ( $mol\ kg_{H_2O}^{-1}\ s^{-1}$ ) corresponding to the sum of the precipitation rate of  
 188 the two endmembers ( $^{235}UO_{2(s)}r$  and  $^{238}UO_{2(s)}r$ )

$$189 \quad ^{ss}r = ^{235}UO_{2(s)}r + ^{238}UO_{2(s)}r \quad (5)$$

190 The precipitation rate for the  $^{235}UO_{2(s)}$  and  $^{238}UO_{2(s)}$  endmembers is calculated according to a  
 191 transition state theory type rate law

$$192 \quad ^{235}UO_{2(s)}r = A \cdot k \left( 1 - \frac{Q_{^{235}UO_{2(s)}}}{K_{^{235}UO_{2(s)}}} \right) + k_{UO_{2(s)}} \cdot A \left( x_{^{235}UO_{2(s)}} - 1 \right) \quad (6)$$

$$193 \quad ^{238}UO_{2(s)}r = A \cdot k \left( 1 - \frac{Q_{^{238}UO_{2(s)}}}{K_{^{238}UO_{2(s)}}} \right) + k_{UO_{2(s)}} \cdot A \left( x_{^{238}UO_{2(s)}} - 1 \right) \quad (7)$$

194 where  $A$  ( $m^2_{\text{mineral}}/kg_{H_2O}$ ) and  $k_{UO_{2(s)}}$  ( $mol\ kg_{H_2O}^{-1}\ m^{-2}\ s^{-1}$ ) refer to the reactive surface area and  
 195 the reaction rate constant of the solid solution, respectively (Table S3),  $Q_{^{235}UO_{2(s)}}$  and  $Q_{^{238}UO_{2(s)}}$   
 196 are the ion activity products of reactions 3 and 4,  $K_{^{235}UO_{2(s)}}$  and  $K_{^{238}UO_{2(s)}}$  refer to the

197 corresponding equilibrium constants (Table S3), and  $x_{235UO_2(s)}$  and  $x_{238UO_2(s)}$  are the mole  
 198 fractions of the precipitating end-members. To ensure that the volume ratio of these endmembers  
 199 reflect the fluid composition,  $x_{235UO_2(s)}$  and  $x_{238UO_2(s)}$  are calculated according to

$$200 \quad x_{235UO_2(s)} = \frac{Q_{235UO_2(s)} / K_{235UO_2(s)}}{Q_{235UO_2(s)} / K_{235UO_2(s)} + Q_{238UO_2(s)} / K_{238UO_2(s)}} \quad (8)$$

201

$$202 \quad x_{238UO_2(s)} = \frac{Q_{238UO_2(s)} / K_{238UO_2(s)}}{Q_{235UO_2(s)} / K_{235UO_2(s)} + Q_{238UO_2(s)} / K_{238UO_2(s)}} \quad (9)$$

203 By setting  $K_{238UO_2(s)}/K_{235UO_2(s)} = 1.001$  and by using a constant reactive surface area  $A$  and a  
 204 reaction rate constant  $k_{UO_2(s)}$  (eqs. (6) and (7)) we run our simulations with an intrinsic  
 205 equilibrium  $\epsilon$  of 1.0‰ (Table S3).

### 206 *Initial conditions*

207 The chemical composition initially specified for the three regions of the model (Fig. 1) as well as  
 208 the variation of the uraninite reaction rate constant with decreasing  $U(VI)_{t=0}$  are listed in Tables  
 209 S4 and S5.

## 210 RESULTS AND DISCUSSIONS

### 211 *U concentration and Isotopic measurements*

212 The U(VI) concentrations and  $\delta^{238}U$  measured at regular time intervals in batch incubations are  
 213 shown in Fig. 2. No significant U(VI) removal in control experiments indicates that the test  
 214 medium does not abiotically reduce U(VI). The X-ray Absorption Near Edge Structure  
 215 (XANES) analysis of the solid reaction products from the experiments confirms that ~90% of the  
 216 U is reduced to U(IV) (Fig. 3). A first order kinetic model reasonably fits the U(VI)  
 217 concentration data from each reactor, except for the latest time points. The half-lives of U(VI)

218 ( $t_{1/2} = \ln(2)/k$ ,  $k$  = first-order rate constant) range from 15 h to 45 h. The normalized first-order  
219 rate constants [ $k_{\text{norm}}$ , defined as  $k_{\text{firstorder}}/(\text{cell density} * U(\text{VI})_{t=0})$ ] vary from 0.0008 to 0.007 h<sup>-1</sup>  
220  $\text{cells}^{-1}\text{mol}^{-1}$  and decrease linearly with increasing initial U(VI) concentration ( $r^2=0.762$ , Fig. S1).

221 The  $\delta^{238}\text{U}$  values of the aqueous U(VI) decreased steadily relative to the starting  $\delta^{238}\text{U}$   
222 composition ( $\sim 0.0\%$ ) to a minimum of  $-1.52\%$  after 67% reduction (Fig. 2, Table S1). The  $\epsilon$   
223 values are determined by fitting the data from each reactor to a Rayleigh distillation model. For  
224 each experiment, a single  $\epsilon$  fits all data from duplicate experiments. The resulting  $\epsilon$  values vary  
225 from 0.36‰ to 0.96‰ (Fig. 2, Table S1) and decrease linearly with increasing  $k_{\text{norm}}$  ( $r^2=0.789$ ,  
226 Fig. 4), meaning that slower U(VI) reduction yields stronger isotopic fractionation. The  
227 uncertainties ( $2\sigma$ ) of  $\epsilon$  values of the duplicate experiments combined range from  $\pm 0.07$  to  
228  $\pm 0.16\%$ .

### 229 ***Reactive transport modeling results***

230 The first simulation is performed for an initial U(VI) concentration ( $^{238}\text{U}(\text{VI}) + ^{235}\text{U}(\text{VI})$ ) of 18  
231  $\mu\text{M}$  while the initial  $\delta^{238}\text{U}$  value is set to 0.0‰ according to the starting  $\delta^{238}\text{U}$  of U(VI). An  
232 intrinsic  $\epsilon$  of 1.0‰ is defined for enzymatic U(VI) reduction, which roughly corresponds to the  
233 maximum  $\epsilon$  observed in our experiments. The chemical composition initially specified for the  
234 three regions of the model is given in Table S4. The diffusion coefficients for  $^{235}\text{U}(\text{VI})$ ,  $^{238}\text{U}(\text{VI})$ ,  
235 and all other aqueous species are set to  $10^{-9} \text{ m}^2 \text{ s}^{-1}$ . A good match between experimental data and  
236 simulation results is achieved by numerically calibrating the rate constant of the specified U(VI)  
237 reduction reaction and the tortuosity of the boundary layer (Fig. 5, 6).

238 After calibrating the model, simulations are run for initial U(VI) concentrations of 15, 10, and  
239 5  $\mu\text{M}$ . The reaction rate constants for computing U(VI) reduction are adjusted according to the  
240 correlation observed between  $k_{\text{norm}}$  and the initial U(VI) concentration (Fig. S1). All other

241 parameters are kept the same as in the simulations performed for  $U(VI)_{t=0} = 18 \mu\text{M}$ . For all initial  
242  $U(VI)$  concentrations,  $\delta^{238}\text{U}$  decreases with progressive  $U(VI)$  reduction. When plotted against  
243 the fraction of reduction ( $\ln(f)$ ), simulated  $\delta^{238}\text{U}$  values in the bulk region plot on perfectly  
244 straight lines ( $r^2=1$ ) (Fig. 7). This demonstrates that  $U$  isotopic fractionation during  $U(VI)$   
245 reduction follows a Rayleigh type distillation with an effective  $\epsilon$  that varies between the  
246 simulations despite defining a constant input  $\epsilon$  of 1.0‰. Therefore, a Rayleigh type model is  
247 applied to calculate the effective  $\epsilon$  for all our simulations, which corresponds to the slope of the  
248 best-fit lines on  $\delta^{238}\text{U}$  vs.  $\ln(f)$  plots. The  $\epsilon$  derived from the simulations also decreases with  
249 increasing  $k_{\text{norm}}$  and matches very well with the  $\epsilon$  derived from the experimental data (Fig. 4).

### 250 ***Rate dependence of U Isotopic fractionation***

251 Similar to microbial S or N isotopic fractionation, the dependence of  $U$  isotopic fractionation  
252 on  $U(VI)$  reduction rate suggests a diffusive barrier between the reaction site and the bulk  $U(VI)$   
253 pool. The diffusive barriers may arise from surface coatings of extracellular polymeric  
254 substances (EPS) enveloping the cell<sup>38-40</sup> or from the cell membrane if a substantial portion of  
255 reduction is intracellular (i.e. occurring in periplasmic space)<sup>21</sup>. Therefore, we hypothesize that  
256 the site of  $U(VI)$  reduction is isolated from the bulk  $U(VI)$  solution by a diffusive boundary layer  
257 around the cells, impacting the overall “effective”  $U$  isotopic fractionation. The generally good  
258 reproduction of observed fractionation factors (Fig. 4) as a function of reaction rate by our  
259 reactive transport simulations provides support for this hypothesis, as we discuss below.

260 In our models, the concentration difference of  $U(VI)$  across the diffusive boundary layer  
261 causes  $U(VI)$  to diffuse across the barrier. Due to reduction, the  $U(VI)$  concentration is lower in  
262 the enzyme region and diffusion of  $U(VI)$  always occurs from the bulk to the enzyme region.  
263 Because the diffusive transport step involves no changes in redox state of  $U$ , it does not

264 significantly discriminate between its isotopologues (i.e.  $^{238}\text{U(VI)}$  and  $^{235}\text{U(VI)}$ ) and causes very  
265 small isotopic fractionation. It simply controls the availability of the U pool to the reduction step.  
266 Therefore, the balance between the kinetics of the diffusion step and the reduction step becomes  
267 very important and controls the overall isotopic fractionation. To further discuss this balance, we  
268 use two endmember scenarios as examples.

269 First, consider an endmember case of a very rapid enzymatic reduction. Here, diffusion of  
270 U(VI) through the boundary layer is the rate-limiting step of all the steps involved in the U(VI)  
271 reduction process. The concentrations of both  $^{238}\text{U(VI)}$  and  $^{235}\text{U(VI)}$  in the remaining U(VI)  
272 around the enzyme quickly approach zero. As a consequence, a strong U(VI) concentration  
273 gradient develops across the boundary layer and the ratio of the concentration gradients for  
274  $^{238}\text{U(VI)}$  and  $^{235}\text{U(VI)}$  across the diffusive boundary is close to the  $^{238}\text{U(VI)}/^{235}\text{U(VI)}$  ratio in the  
275 bulk region. Thus, only minor discrimination between  $^{238}\text{U}$  and  $^{235}\text{U}$  occurs during further  
276 diffusive transport. Outside the boundary layer, the  $^{238}\text{U(VI)}/^{235}\text{U(VI)}$  in the bulk region remains  
277 similar to that of the starting U(VI), and only minor effective isotopic fractionation occurs  
278 compared to the intrinsic equilibrium  $\epsilon$  of  $\sim 1\%$  caused by the NVE<sup>4,5</sup>. In the second endmember  
279 case of extremely slow reduction, diffusion of U(VI) becomes much faster than reduction  
280 causing the boundary layer to disappear. As a consequence, the overall isotopic fractionation  
281 approaches intrinsic fractionation.

282 In between these endmember cases where diffusion is not fully rate-limiting, slow enzymatic  
283 reduction results in accumulation of remaining U(VI) reactant at the inside end of the diffusive  
284 boundary layer with an  $^{235}\text{U}$  enrichment determined by the intrinsic  $\epsilon$  for the reduction. Thus, the  
285 overall U(VI) concentration gradient across the boundary layer is less pronounced than in the  
286 first endmember case and the ratio of the concentration gradients for  $^{238}\text{U(VI)}$  and  $^{235}\text{U(VI)}$

287 deviates from that in the initial bulk U(VI). This, in turn, causes a relatively enhanced diffusion  
 288 of  $^{238}\text{U(VI)}$  across the boundary layer. In these scenarios, the reduction of U(VI) on the inside  
 289 end of the diffusive boundary layer will generate an effective isotopic fractionation in the bulk  
 290 U(VI) that is smaller than the intrinsic equilibrium  $\epsilon$  of  $\sim 1\text{‰}$  caused by NVE. Here, the deviation  
 291 from the intrinsic  $\epsilon$  depends on the reduction rate.

292 Eventually, this coupled kinetic-diffusive effect causes a discrimination of U isotopes during  
 293 diffusive transport across the boundary layer and hence observable U isotopic fractionation in the  
 294 bulk region, despite the fact that the diffusivities (i.e. diffusion coefficients) of  $^{238}\text{U(VI)}$  and  
 295  $^{235}\text{U(VI)}$  differ only very slightly. For an additional verification of the consistency of our  
 296 simulations, the proposed diffusion induced fractionation ( $\delta^{238}\text{U}_{\text{diff}}$ ) can be quantified as

$$297 \quad \delta^{238}\text{U}_{\text{diff}} = \left( \frac{R_{\text{gradient}}}{R_{\text{bulk}}} - 1 \right) \cdot 1000 \quad \text{‰} \quad (1)$$

298 where  $R_{\text{gradient}}$  refers to the simulated  $^{238}\text{U(VI)}/^{235}\text{U(VI)}$  ratio of the net diffusive flux across  
 299 the diffusive boundary ( $R_{\text{gradient}} = (d^{238}\text{U(VI)}/dx) / (d^{235}\text{U(VI)}/dx)$ , with  $dx = 20 \text{ nm}$ , Fig. 1), and  
 300  $R_{\text{bulk}}$  refers to the computed  $^{238}\text{U(VI)}/^{235}\text{U(VI)}$  concentration ratio in the bulk region. Physically,  
 301  $\delta^{238}\text{U}_{\text{diff}}$  corresponds to the theoretical U isotopic ratio of the net U(VI) diffusive flux entering  
 302 the cell, after having been diffusively transported across the boundary layer and right before the  
 303 U(VI) reduction step takes place at the enzyme. The computed  $\delta^{238}\text{U}_{\text{diff}}$  values are higher than the  
 304 simulated  $\delta^{238}\text{U}$  values in the bulk region, and plot on Rayleigh distillation models with effective  
 305 enrichment factors that are almost identical to the  $\epsilon$  derived from the simulated  $^{238}\text{U(VI)}$  and  
 306  $^{235}\text{U(VI)}$  concentrations in the bulk region (shown by the dotted line, Fig. 7). This verifies that  
 307 the observed and simulated variation in  $\epsilon$  (Fig. 2, 7) is mainly due to a preferred diffusion  
 308 induced fractionation of  $^{238}\text{U(VI)}$  across the boundary layer.

309 A similar weakening of isotopic fractionation, sometimes described as reservoir effect, has  
310 been reported for reduction Se(VI) in sediments of littoral wetland<sup>10</sup>. This phenomenon arising  
311 from diffusive limitations within isolated zones of Se(VI) reduction in sediments lowers the  
312 effective  $\epsilon$  observed in Se(VI) in overlying water as a function of the distance across which  
313 Se(VI) diffuses to the reaction sites. Although the conceptual approach is similar with regards to  
314 the isolation of reaction sites in the enzyme region, our data can be explained by a diffusion  
315 induced fractionation of U isotopes as described above. Furthermore, in our model we vary the  
316 U(VI) reduction rate while keeping the length of the diffusive boundary the same. Note that there  
317 is no to back diffusion of <sup>235</sup>U enriched U(VI) from the enzyme to the bulk region, which would  
318 have to occur against the U concentration gradient. Our results identify U(VI) reaction rate as a  
319 crucial factor that controls the effective  $\epsilon$  measured in the bulk region.

320 It is possible to invoke the sequestration of U as U(VI) via adsorption on the cells or as U(VI)  
321 solid phases inside the cell prior to reduction as an alternative reaction mechanism that may  
322 explain our observations of muted isotopic fractionation from *Shewanella* sp. (NR) experiments.  
323 U(VI) removal from the solution via adsorption, however, preferentially removes <sup>235</sup>U<sup>41,43</sup>, which  
324 is inconsistent with our data (Fig. 2). Moreover, the adsorption of U(VI) on microbial cells is  
325 unlikely to be the major U removal mechanism due to presence of U(VI)-complexing anions (1  
326 mM Ca, 10 mM HCO<sub>3</sub><sup>-</sup>) and low cell density (~10<sup>7</sup> cells/mL or less) in all of our experiments.  
327 Finally, the first order kinetics of U(VI) removal throughout the course of all experiments  
328 suggest a single removal mechanism, which is identified as reduction by the XANES data. Even  
329 if some of the U(VI) is adsorbed onto the cell at some point in its journey from bulk solution  
330 across the boundary layer, any isotopic fractionation in the opposite direction (i.e., <sup>238</sup>U  
331 enrichment in bulk U(VI)) during this sorption does not affect our interpretation because of the

332 following reason. Manifestation of U isotopic fractionation in the dissolved U(VI) requires an  
333 exchange between U(VI) and U(IV) via reversible weak sorption of U(VI)<sup>24</sup>, so eventual  
334 desorption reverses any isotopic fractionation caused by sorption of U(VI). Therefore, we  
335 conclude that such a sorption effect is likely negligible.

336 Based on our results, U isotopic fractionation should be influenced by both the rate and the  
337 mechanism of U(VI) reduction. Our conceptual model of a diffusive boundary layer around the  
338 bacterial cells and simulation results successfully explain how the rate of U(VI) reduction  
339 controls U isotopic fractionation during microbial U(VI) reduction. It should be noted that our  
340 model does not consider the role of the reduction mechanism in influencing the U isotopic  
341 fractionation. The mechanism of U(VI) reduction is likely to vary with reductants with varying  
342 electron donating capacity, bonding environment and consequent changes in free energy of the  
343 reaction. Previous studies have extended Marcus theory to show that the kinetic isotopic  
344 fractionation during redox reactions is related to both reaction kinetics and the vibrational energy  
345 differences between reactants and products and thus reaction mechanism and equilibrium  
346 fractionation factors<sup>43,44</sup>. According to Marcus theory, the logarithm of the rate constant of redox  
347 reactions ( $\ln(k)$ ) varies linearly with the free energy change of the reaction ( $\Delta G_r^0$ )<sup>43-48</sup>. This  
348 means that thermodynamically more favorable reactions at higher  $\Delta G_r^0$  are faster and have lower  
349 activation energy differences between two isotopologues, which should yield smaller  
350 fractionation. In future studies, the idea of integrating both the kinetics of electron transfer and  
351 equilibrium exchange should be considered to explain overall observed U isotope fractionation<sup>48</sup>  
352 in addition to the presence of diffusive boundary layers as we have discussed above. Moreover, it  
353 could be assessed whether a coupled kinetic-equilibrium effect as derived from Marcus theory is

354 responsible for observing an equilibrium nuclear volume effect (preference of  $^{238}\text{U}$  in U(IV))  
355 also in kinetically controlled U(VI) reduction experiments such as in the present study.

### 356 ***Environmental Implications***

357 Our rate dependent model of microbial U isotope fractionation may be used to interpret  
358 environmental U isotope data from a range of settings based on variable abundance of organic  
359 matter or electron donors. Our model predicts a small and perhaps variable effective  
360 fractionation during active bioremediation experiments where the amended organic carbon  
361 enhances the U(VI) reduction rate<sup>9,49</sup>. For instance, this is consistent with a rather low effective  $\epsilon$   
362 of 0.46‰ reported for an early stage of the Rifle biostimulation experiment<sup>9</sup>. A recent and more  
363 detailed study with a richer dataset at the same site has reported effective  $\epsilon$  ranging from 0.65‰  
364 to 0.85‰ with changing acetate concentrations (4–15 mM) and hence variable U(VI) reduction  
365 rates<sup>25</sup>. Although the correlation between reported  $\epsilon$  and U(VI) reduction rate is not perfect  
366 because the field experiment is far more complex than a well-mixed batch reactor, this study  
367 confirms that U isotopic fractionation does indeed vary at the field-scale when U(VI) reduction  
368 rates are changing. In contrast, in natural situations like marine and terrestrial sediments with low  
369 organic carbon contents, a slow U(VI) reduction rate should produce a larger fractionation  
370 approaching a theoretical NVE value of  $\sim 1\%$ <sup>4,5</sup>. For example, at Smith Ranch-Highlands roll-  
371 front deposits, with sub-micromolar dissolved U(VI)<sup>5</sup> and generally low organic C content of the  
372 host sediments<sup>50</sup>, as well as the lack of a sharp redox gradient evident from a microbial  
373 community with diverse and competing metabolism<sup>51</sup>, U(VI) reduction is likely slow. This is  
374 consistent with a rather high effective  $\epsilon$  value of 0.8‰ inferred from variations in the  $\delta^{238}\text{U}$  of  
375 groundwater at the Smith Ranch-Highlands U mine<sup>7</sup> where a significant fraction of the U(VI)  
376 reduction is proposed to be microbially mediated<sup>51,52</sup>. The agreement between the fractionation

377 regime suggested by our model at high and low U(VI) reduction rates and the observed  $\epsilon$  from  
378 the field sites with high and low U(VI) reduction rate demonstrate a systematic relationship  
379 between  $k_{\text{norm}}$  and  $\epsilon$  that may be extended to a wider range of natural settings. If either  $\epsilon$  or U(VI)  
380 reduction rate is directly measured, the systematic relationship may be used to predict the other  
381 one. Therefore, direct measurements of U isotope ratios provide a way to quantify U(VI)  
382 reduction rate, which is particularly difficult to quantify in modern open systems or in the past  
383 environments from the rock record.

384

385 ASSOCIATED CONTENT

386 **Supporting Information.** U(VI) concentration and U isotope results from bacterial incubations,  
387 physical and initial chemical parameters for the multi-region model, thermodynamic and kinetic  
388 parameters for U(VI) reduction reactions, reaction rate constants to simulate U(VI) reduction,  
389 and correlations between normalized U(VI) reduction rate constants and initial U(VI)  
390 concentrations are provided in the Supporting Information.

391 AUTHOR INFORMATION

392 **Corresponding Author**

393 \* Anirban Basu ([Anirban.Basu@rhul.ac.uk](mailto:Anirban.Basu@rhul.ac.uk)), Department of Earth Sciences, 251 Queens  
394 Building, Royal Holloway, University of London, Egham, Surrey, UK, TW20 0EX, +44 (0)1784  
395 443890; FAX +44 (0) 1784 471 780

396 **Author Contributions**

397 The manuscript was written through contributions of all authors.  
398 All authors have given approval to the final version of the  
399 manuscript.

#### 400 ACKNOWLEDGMENT

401 This work was supported by the U.S. Department of Energy (USDOE), Office of Science  
402 within the Subsurface Biogeochemical Research (SBR) Program under grant DE-SC0001281.  
403 We thank the MRCAT/EnviroCAT beamline staff for assistance during XAFS data collection.  
404 The XAFS data collection at the Advanced Photon Source and analyses and effort of KMK and  
405 MIB were supported by the Argonne Wetlands Hydrobiogeochemistry Scientific Focus Area  
406 (SFA) at Argonne National Laboratory funded by the SBR Program, Office of Biological and  
407 Environmental Research, Office of Science, USDOE, under contract DE-AC02-06CH11357.  
408 MRCAT/EnviroCAT operations are supported by DOE and the MRCAT/EnviroCAT member  
409 institutions. We thank the anonymous reviewers for their insightful comments.

410  
411

#### 412 REFERENCES

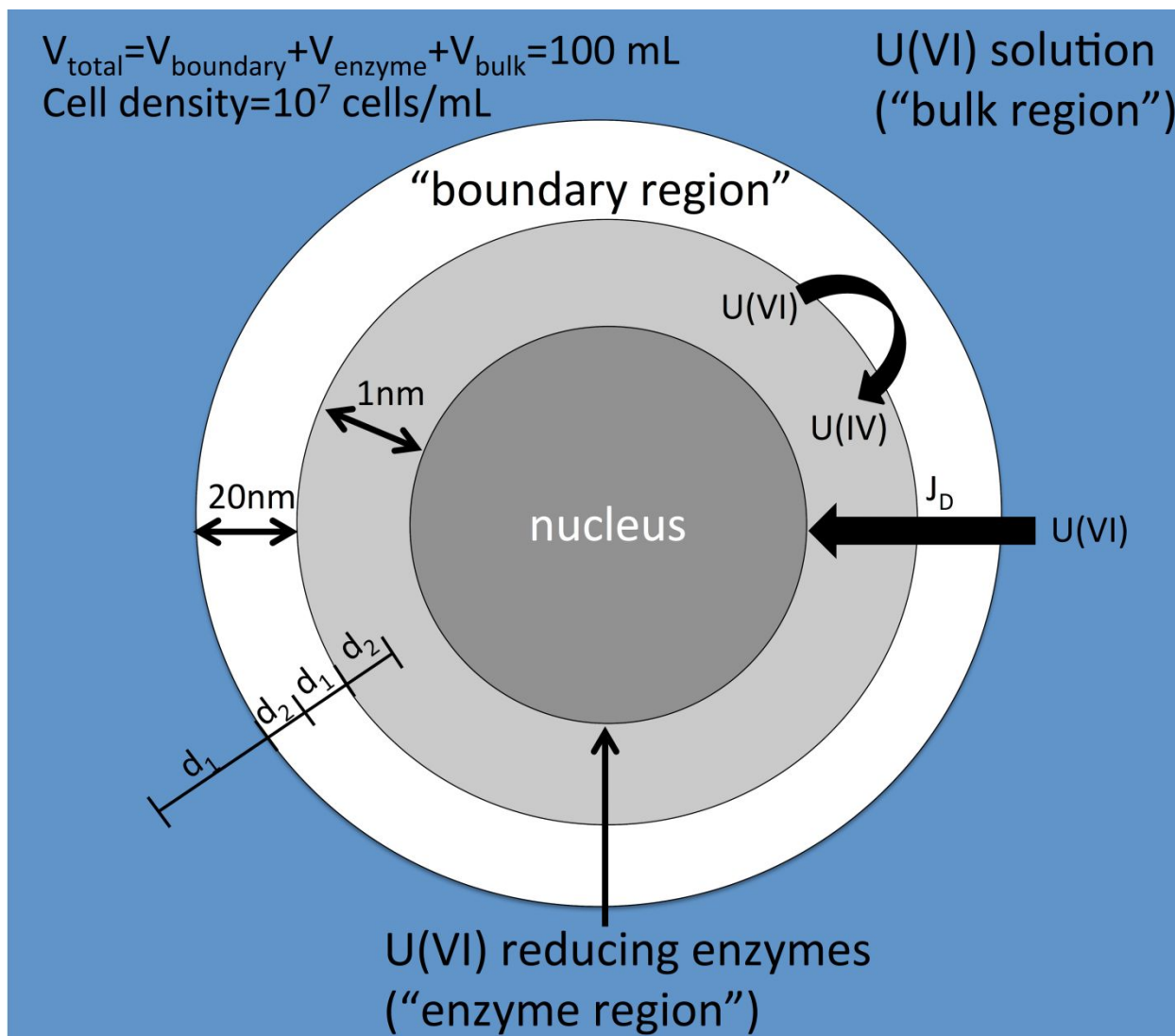
- 413
- 414 1. Basu, A., Sanford, R. A., Johnson, T. M., Lundstrom, C. C., Löffler, F. E. Uranium  
415 isotopic fractionation factors during U(VI) reduction by bacterial isolates. *Geochim.*  
416 *Cosmochim. Acta* **2014**, *136*, 100–113.
  - 417 2. Stylo, M., Neubert N., Wang, Y., Monga, N., Romaniello, S.J., Weyer, S., Bernier-  
418 Latmani, R. Uranium isotopes fingerprint biotic reduction. *Proc. Natl. Acad. Sci. U.S.A.*  
419 **2015**, *112*. 5619-5624.
  - 420 3. Stirling, C. H., Andersen, M. B., Warthmann, R., Halliday, A. N. Isotope fractionation  
421 of  $^{238}\text{U}$  and  $^{235}\text{U}$  during biologically-mediated uranium reduction. *Geochim. Cosmochim.*  
422 *Acta* **2015**, *163*, 200–218.
  - 423 4. Bigeleisen, J. Nuclear size and shape effects in chemical reactions. Isotope chemistry of  
424 the heavy elements. *J. Am. Chem. Soc.* **1996**, *118*, 3676–3680.
  - 425 5. Fujii, T., Moynier, F., Albarède, F. The nuclear field shift effect in chemical exchange  
426 reactions. *Chem. Geol.* **2009**, *267*, 139–156.
  - 427 6. Basu, A., Brown, S. T., Christensen, J. N., DePaolo, D. J., Reimus, P. W., Heikoop, J.

- 428 M., Woldegabriel, G., Simmons, A. M., House, B. M., Hartmann, M., Maher, K.  
429 Isotopic and geochemical tracers for U(VI) reduction and U mobility at an in situ  
430 recovery U mine. *Environ. Sci. Technol.* **2015**, *49*, 5939–5947.
- 431 7. Brown, S. T., Basu, A., Christensen, J. N., Reimus, P. W., Heikoop, J., Simmons, A.,  
432 Woldegabriel, G., Maher, K., Weaver, K., Clay, J., DePaolo, D. J. Isotopic evidence for  
433 reductive immobilization of uranium across a roll-front mineral deposit. *Environ. Sci.*  
434 *Technol.* **2016**, *50*, 6189–6198.
- 435 8. Lau, K. V., Maher, K., Altiner, D., Kelley, B. M., Kump, L. R., Lehrmann, D. J., Silva-  
436 Tamayo, J. C., Weaver, K. L., Yu, M., Payne, J. L. Marine anoxia and delayed Earth  
437 system recovery after the end-Permian extinction. *Proc. Natl. Acad. Sci. U.S.A.* **2016**,  
438 *113*, 2360–2365.
- 439 9. Bopp, C. J. IV, Lundstrom, C. C., Johnson, T. M., Sanford, R. A., Long, P. E., Williams,  
440 K. H. Uranium  $^{238}\text{U}/^{235}\text{U}$  isotope ratios as indicators of reduction: Results from an in  
441 situ biostimulation experiment at Rifle, Colorado, U.S.A. *Environ. Sci. Technol.* **2010**,  
442 *44*, 5927–5933.
- 443 10. Clark, S. K., Johnson, T. M. Effective isotopic fractionation factors for solute removal  
444 by reactive sediments: A laboratory microcosm and slurry study. *Environ. Sci. Technol.*  
445 **2008**, *42*, 7850–7855.
- 446 11. Wiederhold, J. G. Metal stable isotope signatures as tracers in environmental  
447 geochemistry. *Environ. Sci. Technol.* **2015**, *49*, 2606–2624.
- 448 12. Andersen, M. B., Romaniello, S., Vance, D., Little, S. H., Herdman, R., Lyons, T. W. A  
449 modern framework for the interpretation of  $^{238}\text{U}/^{235}\text{U}$  in studies of ancient ocean redox.  
450 *Earth Planet. Sci. Lett.* **2014**, *400*, 184–194.
- 451 13. Bradley, A. S., Leavitt, W. D., Schmidt, M., Knoll, A. H., Girguis, P. R., Johnston, D. T.  
452 Patterns of sulfur isotope fractionation during microbial sulfate reduction. *Geobiology*  
453 **2015**, *14*, 91–101.
- 454 14. Granger, J., Sigman, D. M., Lehmann, M. F., Tortell, P. D. Nitrogen and oxygen isotope  
455 fractionation during dissimilatory nitrate reduction by denitrifying bacteria. *Limnol.*  
456 *Oceanogr.* **2008**, *53*, 2533–2545.
- 457 15. Bradley, A. S., Leavitt, W. D., Johnston, D. T. Revisiting the dissimilatory sulfate  
458 reduction pathway. *Geobiology* **2011**, *9*, 446–457 (2011).
- 459 16. Santos, A. A., Venceslau, S. S., Grein, F., Leavitt, W. D., Dahl, C., Johnston, D. T.,  
460 Pereira, I. A. C. A protein trisulfide couples dissimilatory sulfate reduction to energy  
461 conservation. *Science* **2015**, *350*, 1541–1545.
- 462 17. Leavitt, W. D., Halevy, I., Bradley, A. S., Johnston, D. T. Influence of sulfate reduction  
463 rates on the Phanerozoic sulfur isotope record. *Proc. Natl. Acad. Sci. U.S.A.* **2013**, *110*,  
464 11244–11249.
- 465 18. Meyer, T. E., Tsapin, A. I., Vandenberghe, I., Smet, L. D., Frishman, D., Nealson, K. H.,  
466 Cusanovich, M. A., Van Beeumen, J. J. Identification of 42 possible cytochrome c genes  
467 in the *Shewanella oneidensis* genome and characterization of six soluble cytochromes.  
468 *OMICS* **2004**, *8*, 57–77.
- 469 19. DiChristina, T. J. Enzymology of electron transport: Energy generation with  
470 geochemical consequences. *Rev. Mineral. Geochem.* **2005**, *59*, 27–52.
- 471 20. DiChristina, T. J., Bates, D. J., Burns, J. L., Dale, J. R., Payne, A. N. *Shewanella*: novel  
472 strategies for anaerobic respiration. In *Past and Present Water Column Anoxia*; Neretin,  
473 L.N. Ed.; SpringerL: Netherlands, 2006; 443–469.

- 474 21. Marshall, M. J., Beliaev, A. S., Dohnalkova, A. C., Kennedy, D. W., Shi, L., Wang, Z.,  
475 Boyanov, M. I., Lai, B., Kemner, K. M., McLean, J. S., Reed, S. B., Culley, D. E.,  
476 Bailey, V. L., Simonson, C. J., Saffarini, D. A., Romine, M. F., Zachara, J. M.,  
477 Fredrickson, J. K. c-type cytochrome-dependent formation of U(IV) nanoparticles by  
478 *Shewanella oneidensis*. *Plos Biol.* **2006**, *4*, e268.
- 479 22. Wall, J. D., Krumholz, L. R. Uranium reduction. *Annu. Rev. Microbiol.* **2006**, *60*, 149–  
480 166.
- 481 23. Liu, C., Zachara, J. M., Fredrickson, J. K., Kennedy, D. W., Dohnalkova, A. Modeling  
482 the inhibition of the bacterial reduction of U(VI) by  $\beta$ -MnO<sub>2</sub>(s). *Environ. Sci. Technol.*  
483 **2002**, *36*, 1452–1459.
- 484 24. Brown, S. T., Basu, A., Ding, X., Christensen, J. N., DePaolo, D. J. Uranium isotope  
485 fractionation by abiotic reductive precipitation. *Proc. Natl. Acad. Sci. U.S.A.* **2018**, *115*,  
486 8688–8693.
- 487 25. Shiel, A. E., Johnson, T. M., Lundstrom, C. C., Laubach, P. G., Long, P. E., Williams,  
488 K. H. Reactive transport of uranium in a groundwater bioreduction study: Insights from  
489 high-temporal resolution <sup>238</sup>U/<sup>235</sup>U data. *Geochim. Cosmochim. Acta* **2016**, *187*, 218–  
490 236.
- 491 26. Hyslop, N. P., White, W. H. Estimating precision using duplicate measurements. *J. Air*  
492 *Waste Manag. Assoc.* **2009**, *59*, 1032–1039.
- 493 27. Scott, K. M., Lu, X., Cavanaugh, C. M., Liu, J. S. Optimal methods for estimating  
494 kinetic isotope effects from different forms of the Rayleigh distillation equation.  
495 *Geochim. Cosmochim. Acta* **2004**, *68*, 433–442.
- 496 28. Boyanov, M. I., Fletcher, K. E., Kwon, M. J., Rui, X., O’Loughlin, E. J., Löffler, F. E.,  
497 Kemner, K. M. Solution and microbial controls on the formation of reduced U(IV)  
498 species. *Environ. Sci. Technol.* **2011**, *45*, 8336–8344.
- 499 29. Xu, T., Sonnenthal, E., Spycher, N. F., Zheng, L. *TOUGHREACT V3.0-OMP Reference*  
500 *manual: a parallel simulation program for non-isothermal multiphase geochemical*  
501 *reactive transport*. Earth Sciences Division, Lawrence Berkeley National Laboratory  
502 University of California, Berkeley, CA 94720;  
503 [http://tough.lbl.gov/assets/docs/TOUGHREACT\\_V3-OMP\\_RefManual.pdf](http://tough.lbl.gov/assets/docs/TOUGHREACT_V3-OMP_RefManual.pdf).
- 504 30. Wolery, T. J. *EQ3/6: software package for geochemical modeling of aqueous systems:*  
505 *package overview and installation guide (version 7.0)*. Lawrence Livermore National  
506 Laboratory Report UCRL-MA-110662 PT I. Livermore, California, 1992.
- 507 31. Spycher, N. F., Issarangkun, M., Stewart, B. D., Şengör, S. S., Belding, E., Ginn, T. R.,  
508 Peyton, B. M., Sani, R. K. Biogenic uraninite precipitation and its reoxidation by  
509 iron(III) (hydr)oxides: A reaction modeling approach. *Geochim. Cosmochim. Acta* **2011**,  
510 *75*, 4426–4440.
- 511 32. Wanner, C., Sonnenthal, E. L. Assessing the control on the effective kinetic Cr isotope  
512 fractionation factor: A reactive transport modeling approach. *Chem. Geol.* **2013**, *337*–  
513 *338*, 88–98.
- 514 33. Singleton, M. J., Sonnenthal, E. L., Conrad, M. E., DePaolo, D. J., Gee, G. W.  
515 Multiphase reactive transport modeling of seasonal infiltration events and stable isotope  
516 fractionation in unsaturated zone pore water and vapor at the Hanford site. *Vadose Zone*  
517 *J.* **2004**, *3*, 775–785.
- 518 34. Wanner, C., Druhan, J. L., Amos, R. T., Alt-Epping, P., Steefel, C. I. Benchmarking the  
519 simulation of Cr isotope fractionation. *Comput Geosci* **2014**, *19*, 497–521.

- 520 35. Xu, T. Incorporating aqueous reaction kinetics and biodegradation into TOUGHREACT:  
521 Applying a multiregion model to hydrobiogeochemical transport of denitrification and  
522 sulfate reduction. *Vadose Zone J.* **2008**, *7*, 305–315.
- 523 36. Abboud, R., Popa, R., Souza-Egipsy, V., Giometti, C. S., Tollaksen, S., Mosher, J. J.,  
524 Findlay, R. H., Nealon, K. H. Low-temperature growth of *Shewanella oneidensis* MR-  
525 1. *Appl. Environ. Microbiol.* **2005**, *71*, 811–816.
- 526 37. Phillips, R. Membranes by the numbers. In *Physics of Biological Membranes*;  
527 Bassereau, P., Sens, P., Eds.; Springer International Publishing, 2018; pp 73–105.
- 528 38. Xiao, Y., Zhang, E., Zhang, J., Dai, Y., Yang, Z., Christensen, H. E. M., Ulstrup, J.,  
529 Zhao, F. Extracellular polymeric substances are transient media for microbial  
530 extracellular electron transfer. *Sci. Adv.* **2017**, *3*(7), e1700623. DOI:  
531 10.1126/sciadv.1700623.
- 532 39. Li, S.-W., Sheng, G.-P., Cheng, Y.-Y., Yu, H.-Q. Redox properties of extracellular  
533 polymeric substances (EPS) from electroactive bacteria. *Sci. Rep.* **2016**, *6*, 39098. DOI:  
534 10.1038/srep39098.
- 535 40. Gao, L., Lu, X., Liu, H., Li, J., Li, W., Song, R., Wang, R., Zhang, D., Zhu, J. Mediation  
536 of extracellular polymeric substances in microbial reduction of hematite by *Shewanella*  
537 *Oneidensis* MR-1. *Front. Microbiol.* **2019**, *10*, 575 (2019).
- 538 41. Brennecka, G. A., Wasylewski, L. E., Bargar, J. R., Weyer, S., Anbar, A. D. Uranium  
539 isotope fractionation during adsorption to Mn-Oxyhydroxides. *Environ. Sci. Technol.*  
540 **2011**, *45*, 1370–1375.
- 541 42. Jemison, N. E., Johnson, T. M., Shiel, A. E., Lundstrom, C. C. Uranium isotopic  
542 fractionation induced by U(VI) adsorption onto common aquifer minerals. *Environ. Sci.*  
543 *Technol.* **2016**, *50*, 12232–12240.
- 544 43. Kavner, A., John, S. G., Sass, S., Boyle, E. A. Redox-driven stable isotope fractionation  
545 in transition metals: Application to Zn electroplating. *Geochim. Cosmochim. Acta* **2008**,  
546 *72*, 1731–1741.
- 547 44. Kavner, A., Bonet, F., Shahar, A., Simon, J., Young, E. The isotopic effects of electron  
548 transfer: An explanation for Fe isotope fractionation in nature. *Geochim. Cosmochim.*  
549 *Acta* **2005**, *69*, 2971–2979.
- 550 45. Marcus, R.A. Chemical and electrochemical electron-transfer theory. *Annu. Rev. Phys.*  
551 *Chem.* **1964**, *15*, 155–196.
- 552 46. Marcus, R. A. Electron transfer reactions in chemistry. Theory and experiment. *Rev.*  
553 *Mod. Phys.* **1993**, *65*, 599–610.
- 554 47. Marcus, R. A. On the Theory of Electron-Transfer Reactions. VI. Unified Treatment for  
555 Homogeneous and Electrode Reactions. *J. Chem. Phys.* **1965**, *43*, 679–701 (1965).
- 556 48. Joe-Wong, C., Weaver, K. L., Brown, S. T., Maher, K. Thermodynamic controls on  
557 redox-driven kinetic stable isotope fractionation. *Geochem. Persp. Lett.* **2019**, *10*, 20–25.
- 558 49. Anderson, R. T., Vrionis, H. A., Ortiz-Bernad, I., Resch, C. T., Long, P. E., Dayvault,  
559 R., Karp, K., Marutzky, S., Metzler, D. R., Peacock, A., White, D. C., Lowe, M.,  
560 Lovley, D. R. Stimulating the in situ activity of *Geobacter* species to remove uranium  
561 from the groundwater of a uranium-contaminated aquifer. *Appl. Environ. Microbiol.*  
562 **2003**, *69*, 5884–5891.
- 563 50. WoldeGabriel, G., Boukhalfa, H., Ware, S. D., Cheshire, M., Reimus, P., Heikoop, J.,  
564 Conradson, S. D., Batuk, O., Havrilla, G., House, B., Simmons, A., Clay, J., Basu, A.,  
565 Christensen, J. N., Brown, S. T., DePaolo, D. J. Characterization of cores from an in-situ

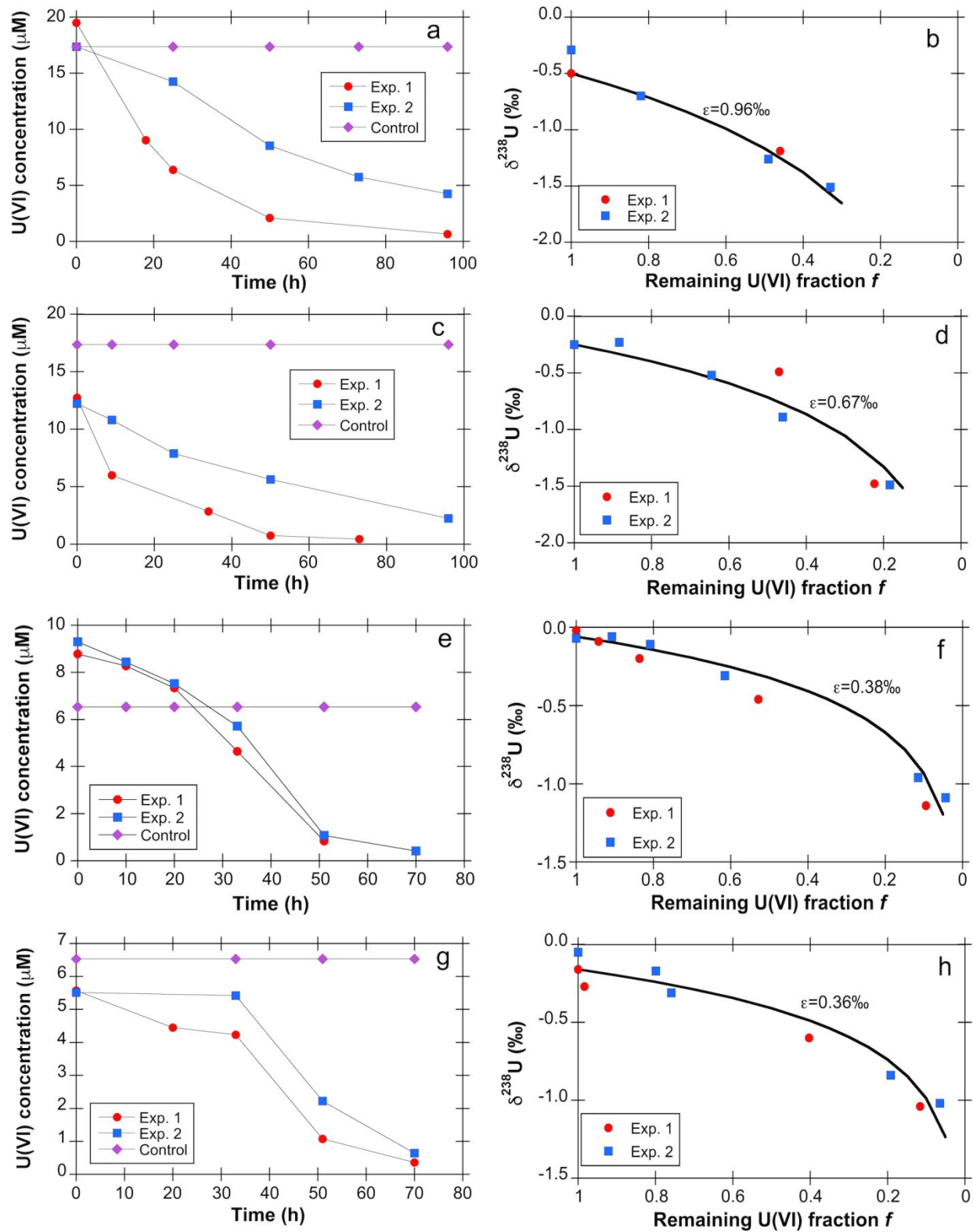
- 566 recovery mined uranium deposit in Wyoming: Implications for post-mining restoration.  
567 *Chem. Geol.* **2013**, *390*, 1–14.
- 568 51. Gallegos, T. J., Campbell, K. M., Zielinski, R. A., Reimus, P. W., Clay, J. T., Janot, N.,  
569 Bargar, J. R., Benzel, W. M. Persistent U(IV) and U(VI) following in-situ recovery  
570 (ISR) mining of a sandstone uranium deposit, Wyoming, USA. *Appl. Geochem.* **2015**,  
571 *63*, 222–234.
- 572 52. Bhattacharyya, A., Campbell, K. M., Kelly, S. D., Roebbert, Y., Weyer, S., Bernier-  
573 Latmani, R., Borch, T. Biogenic non-crystalline U(IV) revealed as major component in  
574 uranium ore deposits. *Nat. Commun.* **2017**, *8*, 1–8.  
575



576  
577

578 **Figure 1.** Conceptual model to simulate U(VI) reduction and associated U isotopic fractionation.

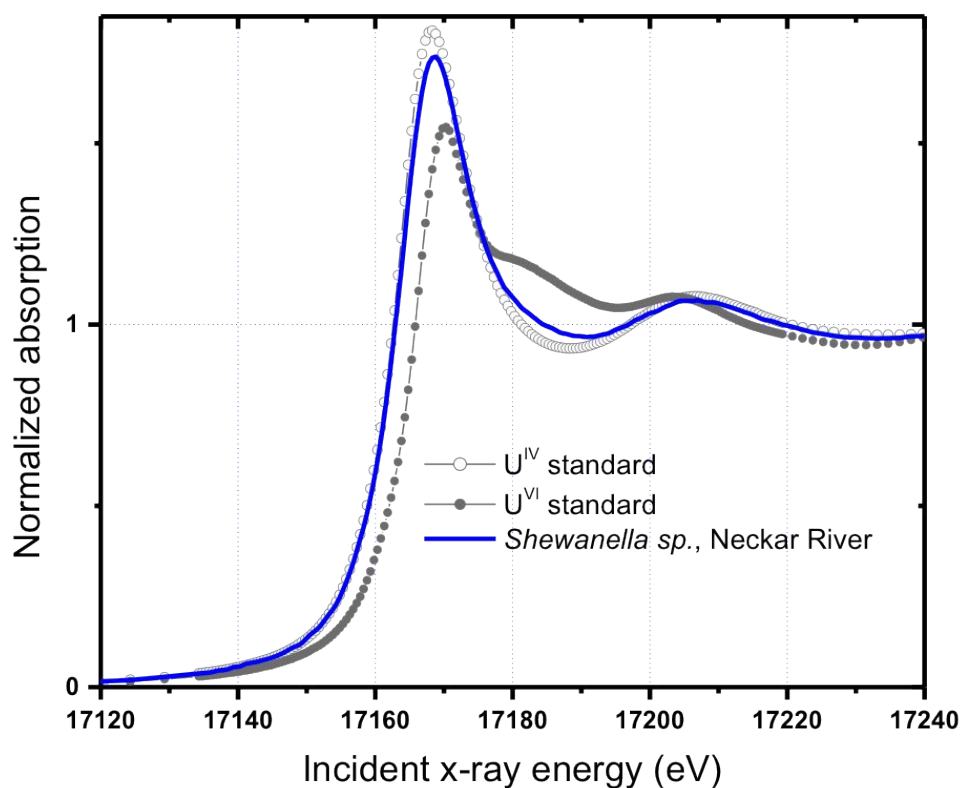
579 The model assumes that U(VI) reduction occurs as a two-step process with (i) diffusive U(VI)  
 580 transport ( $J_D$ ) from the bulk solution (bulk region) to an active site where (ii) enzymatic U(VI)  
 581 reduction is occurring (enzyme region), which may be at the cell surface or within the  
 582 periplasmic space.  $d_1$  and  $d_2$  refer to the distances from the centers of two adjacent regions to  
 583 their mutual interface (Table S2).



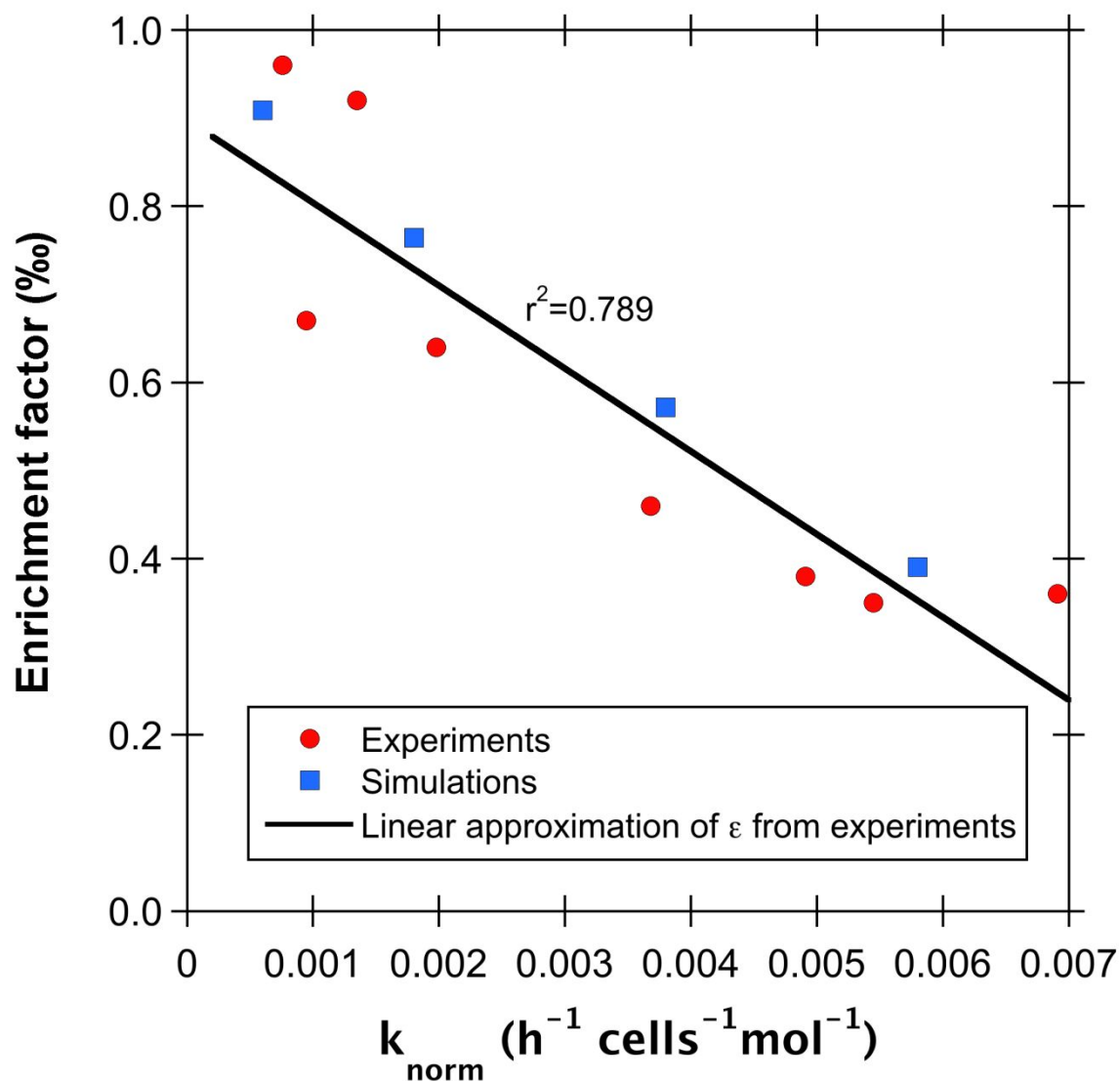
584

585

586 **Figure 2.** The left panel shows U(VI) concentration decrease during incubations with  
 587 *Shewanella sp.* (NR) for U(VI) concentrations a)  $\sim 18.2 \mu\text{M}$  c)  $\sim 12.48 \mu\text{M}$  e)  $\sim 9.04 \mu\text{M}$  g)  $\sim 5.54$   
 588  $\mu\text{M}$ . The right panel shows concomitant U isotopic fractionations in b), d), f), h) and j),  
 589 respectively.  
 590

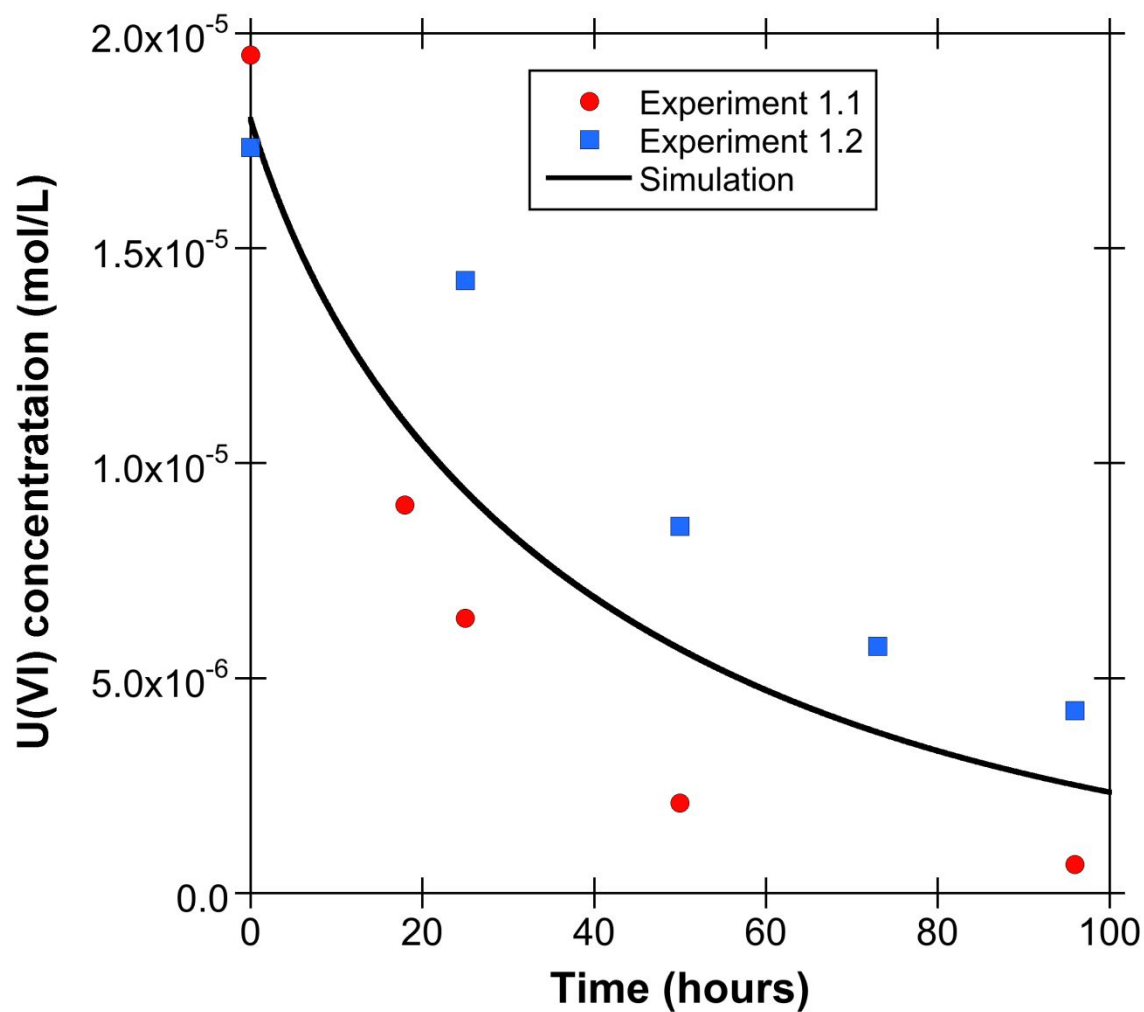


591 **Figure 3.** U  $L_{III}$ -edge XANES spectrum from the solid phase of incubations with *Shewanella sp.*  
 592 (NR) (line), compared to U(VI) and U(IV) standards (symbols). The spectrum overlies the U(IV)  
 593 standard, indicating the predominance of U(IV) species in the sample. The standards are (1)  
 594 aqueous U(VI)-carbonate species and (2) solid-phase U(IV)-phosphate species produced during  
 595 U(VI) reduction by *Desulfitobacterium spp.* More information on these standards can be found in  
 596 ref. <sup>28</sup>.

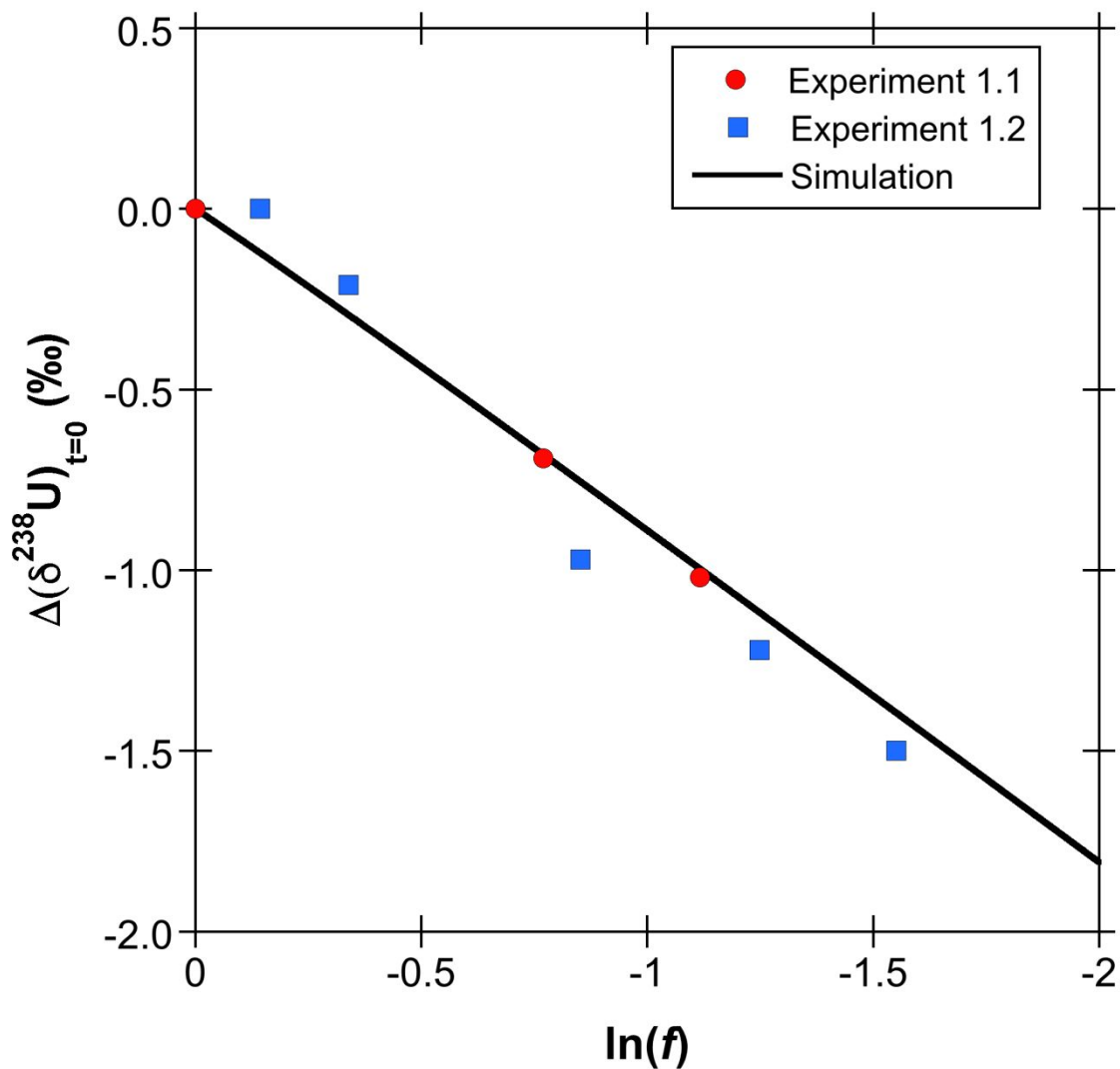


598  
599 **Figure 4 .** Correlations in the U(VI) reduction experiments with *Shewanella* sp. (NR): Isotopic  
600 fractionation  $\epsilon$  vs. normalized rate constant. Also shown are the isotopic fractionation obtained  
601 when running the model with different rate constants for different initial U(VI) concentrations  
602 and hence variable rate constants.

603

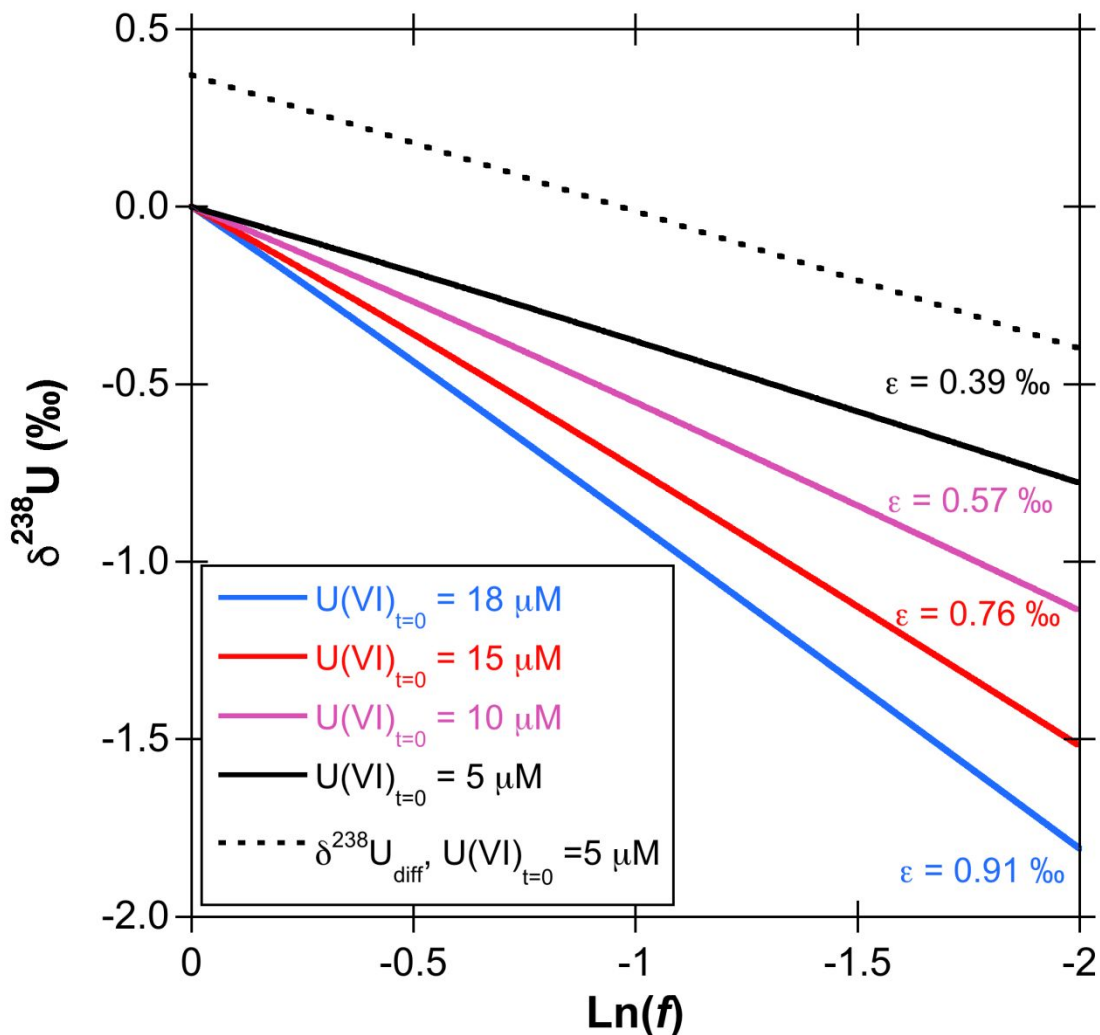


604  
605 **Figure 5.** U(VI) concentration as a function of time obtained for an initial U(VI) concentration  
606 of  $\sim 18 \mu\text{M}$  and corresponding simulation results (bulk region) illustrating successful calibration  
607 of the model.



608  
609

610 **Figure 6.** Relative  $\delta^{238}\text{U}$  changes ( $\Delta(\delta^{238}\text{U})_{t=0}$ ) as a function of the natural logarithm of the  
611 remaining U(VI) fraction  $f$  obtained for an initial U(VI) concentration of  $\sim 18 \mu\text{M}$  and  
612 corresponding simulation results (bulk region) illustrating successful model calibration.



613  
 614 **Figure 7.** Model results (bulk region) for varying initial U(VI) concentrations.  $\delta^{238}\text{U}$  values  
 615 obtained for the bulk region are plotted as a function of the natural logarithm of the remaining  
 616 U(VI) fraction  $f$ . All the simulations plot on perfectly straight lines ( $r^2=1$ ), demonstrating that the  
 617 simulation results follow a Rayleigh type fractionation model with a specific effective epsilon,  
 618 which is expressed by the corresponding slope. For the simulation with a starting U(VI)  
 619 concentration of 5  $\mu\text{M}$ ,  $\delta^{238}\text{U}_{\text{diff}}$  (eq.(1)) is shown as well to demonstrate that diffusion induced  
 620 fractionation causes enrichment of  $^{238}\text{U}(\text{VI})$  across the boundary layer ( $\delta^{238}\text{U}_{\text{diff}} > \delta^{238}\text{U}_{\text{bulk}}$ ) and  
 621 that the corresponding epsilon is equal to the one obtained from the evolution of  $\delta^{238}\text{U}$  in the bulk  
 622 solution.

1  
2  
3  
4  
5  
6  
7  
8  
9  
10  
11  
12  
13  
14  
15  
16  
17  
18  
19  
20  
21  
22

## Supporting Information

# Microbial U isotope fractionation depends on U(VI) reduction rate

*Anirban Basu<sup>1\*</sup>, Christoph Wanner<sup>2</sup>, Thomas M. Johnson<sup>3</sup>, Craig  
C. Lundstrom<sup>3</sup>, Robert A. Sanford<sup>3</sup>, Eric L. Sonnenthal<sup>4</sup>,  
Maxim I. Boyanov<sup>5,6</sup>, Kenneth M. Kemner<sup>5</sup>*

1. Department of Earth Sciences, Royal Holloway, University  
of London, Egham, UK, TW20 0EX

2. Institute of Geological Sciences, University of Bern,  
Baltzerstrasse 3, CH-3012, Switzerland

3. Department of Geology, University of Illinois at Urbana-  
Champaign, Urbana, IL, USA 61801

4. Lawrence Berkeley National Laboratory, 1 Cyclotron Road,  
Berkeley, CA, USA, 94720

5. Biosciences Division, Argonne National Laboratory,  
Argonne, IL, USA, 60439

6. Bulgarian Academy of Sciences, Institute of Chemical  
Engineering, Sofia 1113, Bulgaria

23 Number of pages: 6; Number of Tables: 5; Number of Figures:

24 1

25 Table S1. Results from U(VI) incubations with *Shewanella* sp. (NR).

Time (h)	U(VI) ( $\mu\text{M}$ )	% Removed	$\delta^{238}\text{U}(\text{‰})$	Half-life of U(VI) $\ddagger$
Average initial U(VI) = 18.2 $\mu\text{M}$				
Exp 1				
0	19.50	0%	-0.50‰	19.63 h
18	9.03	54%	-1.19‰	
25	6.39	67%	-1.52‰	
50	2.09	89%	-2.02‰*	
96	0.66	97%	-2.28‰*	
Exp 2				
0	17.35	0%	-0.29‰	44.71 h
25	14.25	18%	-0.70‰	
50	8.53	51%	-1.26‰	
73	5.74	67%	-1.51‰	
96	4.24	76%	-1.79‰	
Average initial U(VI) = 12.48 $\mu\text{M}$				
Exp 1				
0	12.73	0%	-0.25‰	15.10 h
9	5.99	53%	-0.49‰	
34	2.85	78%	-1.48‰	
50	0.75	94%	-1.92‰*	
73	0.45	96%	-1.63‰*	
Exp 2				
0	12.22	0%	-0.25‰	39.60 h
9	10.80	12%	-0.23‰	
25	7.88	36%	-0.52‰	
50	5.63	54%	-0.89‰	
96	2.25	82%	-1.49‰	
Average initial U(VI) = 9.04 $\mu\text{M}$				
Exp 1				
0	8.78	0%	-0.02‰	15.33 h
10	8.27	6%	-0.09‰	
20	7.34	16%	-0.20‰	
33	4.64	47%	-0.46‰	
51	0.83	91%	-1.14‰	
Exp 2				
0	9.30	0%	-0.07‰	14.59 h
10	8.44	9%	-0.06‰	
20	7.52	19%	-0.11‰	
33	5.72	38%	-0.31‰	
51	1.07	88%	-0.96‰	

70	0.41	96%	-1.09‰	
Average initial U(VI) = 5.54 $\mu$ M				
Exp 1				
0	5.57	0%	-0.05‰	
20	4.45	20%	-0.17‰	
33	4.23	24%	-0.31‰	17.03 h
51	1.07	81%	-0.84‰	
70	0.36	94%	-1.02‰	
Exp 2				
0	5.51	0%	-0.16‰	
33	5.42	2%	-0.27‰	23.33 h
51	2.22	60%	-0.60‰	
70	0.64	88%	-1.04‰	

26  
27  
28  
29  
30  
31

‡Half-life of U(VI) =  $\ln(2)/k$ , k = first-order rate constant

\* Not used in calculation of  $\epsilon$

32 Table S2: Physical parameters defined for the three regions of the multi-region model

	Bulk region		Boundary region			Enzyme region
Volume	m <sup>3</sup>	1.00E-04	1.24E-10			8.37E-10
Porosity	-	0.99	0.99			0.99
Distance to interface			d <sub>2</sub>	d <sub>1</sub>	d <sub>2</sub>	d <sub>1</sub>
	nm		7.17E+06	10	10	1
<sup>a</sup> Area between regions	m <sup>2</sup>		6.97E-03		6.47E-03	
Tortuosity	-	<sup>b</sup> 10 <sup>8</sup>	<sup>c</sup> 0.2			<sup>b</sup> 10 <sup>8</sup>

33  
34  
35  
36  
37  
38  
39  
40  
41  
42  
43  
44

<sup>a</sup> Based on cuboid shaped cells with d=0.6 and l=3.4 as well as a cell density of 10<sup>7</sup> cells/mL

<sup>b</sup> Perfect mixing assumed

<sup>c</sup> Calibrated to match experimental data for U(VI)<sub>t=0</sub> = 18  $\mu$ M

45 Table S3: Thermodynamic and kinetic parameters ( $A$ ,  $k$ ) used to  
 46 calculate the reduction of U(VI) and the precipitation of  
 47  $\text{UO}_{2(s)}$

End-member	Reaction stoichiometry	<sup>a</sup> equilibrium constant $\log(K)$	Reactive surface area $A$ ( $\text{m}^2/\text{kg}_{\text{H}_2\text{O}}$ )	Rate constant $k$
$^{235}\text{UO}_{2(s)}$	$^{235}\text{UO}_{2(s)} + 0.5 \text{HCO}_3^- + 0.5 \text{C}_2\text{H}_3\text{O}_2^- + 2.5 \text{H}^+ = 0.5 \text{C}_3\text{H}_5\text{O}_3^- + (^{235}\text{UO}_2)^{2+} + \text{H}_2\text{O}$	-4.9345	2.03E-03	Variable (Table S4)
$^{238}\text{UO}_{2(s)}$	$^{238}\text{UO}_{2(s)} + 0.5 \text{HCO}_3^- + 0.5 \text{C}_2\text{H}_3\text{O}_2^- + 2.5 \text{H}^+ = 0.5 \text{C}_3\text{H}_5\text{O}_3^- + (^{238}\text{UO}_2)^{2+} + \text{H}_2\text{O}$	-4.93406549	2.03E-03	Variable (Table S4)

48 <sup>a</sup> $K_{235\text{UO}_2(s)}/K_{238\text{UO}_2(s)} = 0.999$  refers to the intrinsic equilibrium fractionation factor  
 49 specified for our simulations and corresponds to an intrinsic  $\epsilon$  of 1.0 ‰. Moreover, the  
 50 specified  $\log(K)$  values correspond to a U(IV) solubility controlled by uraninite with a  
 51 grain size of 3 nm as postulated by ref. <sup>1</sup>.

52  
53  
54  
55

56 Table S4: Initial chemical composition specified for the  
 57 three regions of the multi-region model

		Bulk region	Boundary region	Enzyme region
pH	-	7.2	7.2	7.2
$\text{HCO}_3^-$	mol/L	0.001	0.001	0.001
$\text{Na}^+$	mol/L	0.009	0.009	0.009
$^{238}\text{UO}_2^{2+}$	mol/L	1.79E-05 <sup>a</sup>	1.00E-20	1.00E-20
$^{235}\text{UO}_2^{2+}$	mol/L	1.30E-07 <sup>a</sup>	1.00E-20	1.00E-20
Lactic acid	mol/L	5.00E-04	5.00E-04	5.00E-04
Acetic acid	mol/L	1.00E-10	1.00E-10	1.00E-10

58 <sup>a</sup> Varies for different simulation run. Shown here are the concentrations defined for the  
 59 calibration run simulating an initial total U(VI) concentration of 18  $\mu\text{M}$ . Moreover, the  
 60 specification corresponds to  $\delta^{238}\text{U} = 0\text{‰}$

61  
62  
63

64

65 Table S5: Reaction rate constants ( $k_{\text{UO}_2(\text{s})}$ , eqs. (6) and (7))  
 66 specified for simulating U(VI) reduction at variable initial  
 67 U(VI) concentrations

$\text{U(VI)}_{t=0}$ ( $\mu\text{M}$ )	$^{\text{a}}k_{\text{norm}}$ ( $\text{h}^{-1}\text{cells}^{-1}\text{mol}^{-1}$ )	$k_{\text{norm}}$ relative to $\text{U(VI)}_{t=0} = 18 \mu\text{M}$	$^{\text{b}}k_{\text{UO}_2(\text{s})}$ ( $\text{mol kg}_{\text{H}_2\text{O}}^{-1} \text{m}^{-2} \text{s}^{-1}$ )
18	0.0006	1	$^{\text{c}}3.50\text{e-}16$
15	0.0018	3	$^{\text{d}}1.05\text{e-}15$
10	0.0038	6.33	$^{\text{d}}2.21\text{e-}15$
5	0.0058	9.67	$^{\text{d}}3.38\text{e-}15$

68 <sup>a</sup>Calculated using the negative correlation approximated in Fig. S1.

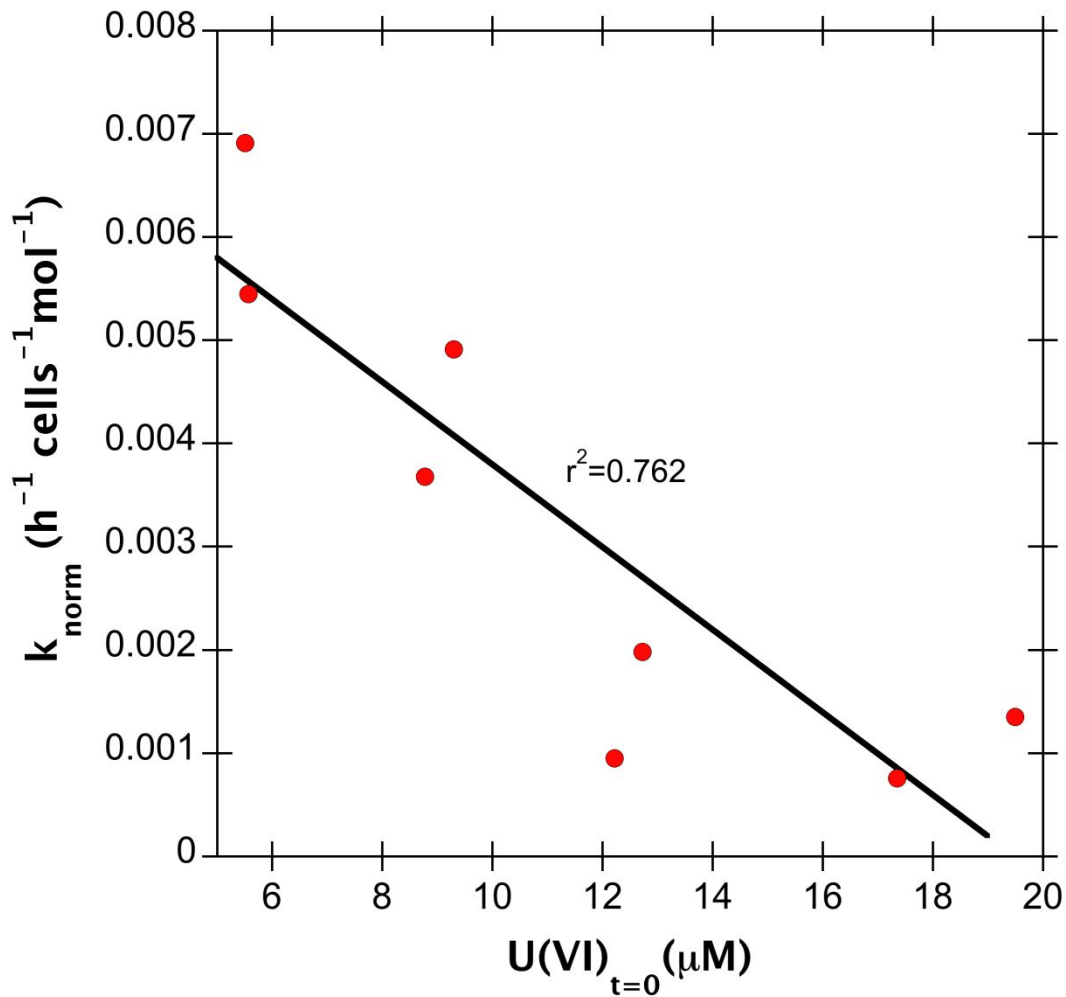
69 <sup>b</sup>The same constant is specified for the two isotopically different  $\text{UO}_2(\text{s})$  endmembers  
 70 (Table S3)

71 <sup>c</sup>Calibrated to match experimental results at an initial U(VI) concentration of  $18 \mu\text{M}$

72 <sup>d</sup>Input value defined for simulating the experiment with initial U(VI) concentrations of  
 73 15, 10 and  $5 \mu\text{M}$

74

75



76  
77

78 **Figure S1.** Correlations in the U(VI) reduction experiments  
79 with *Shewanella* sp. (NR): Normalized rate constant  
80 ( $k_{\text{norm}} = k_{\text{first\_order}} / (\text{cell density} \times U(\text{VI})_{t=0})$ ) vs.  $U(\text{VI})_{t=0}$ .

81

82 REFERENCES

- 83 1. Spycher, N. F., Issarangkun, M., Stewart, B. D., Şengör, S. S., Belding, E., Ginn,  
84 T. R., Peyton, B. M., Sani, R. K. Biogenic uraninite precipitation and its  
85 reoxidation by iron(III) (hydr)oxides: A reaction modeling approach. *Geochim.*  
86 *Cosmochim. Acta* **2011**, *75*, 4426–4440.

87